ORIGINAL ARTICLE
Journal Section

Creating Physically-Coherent and Spatially-Correlated Perturbations to Initialize High-Resolution Ensembles of Simulated Convection

Jonathan D. Labriola[1,2] | **Louis J. Wicker**[2]

[1]National Research Council, Washington, DC, 20001, United States

[2]National Severe Storms Laboratory, Norman, Oklahoma, 73072, United States

Correspondence
Jonathan Labriola, National Severe Storms Laboratory, Norman, Oklahoma, 73072, United States
Email: jonathan.labriola@noaa.gov

Funding information

The use of ensembles for numerical weather prediction has become common during the last decade. For global models, the generation of initial condition perturbations has a number of well-tested methodologies. In ensembles that predict convective storms explicitly (i.e., $\Delta x < 4$ km), the generation of physically realistic perturbations is less well posed. This study introduces a technique to generate physically-coherent and spatially-correlated (PCSC) initial condition perturbations that are calibrated to the environment. Ensembles of idealized CM1 simulations initialized either with PCSC perturbations (EXP_PCSC), spatially coherent random perturbations (EXP_3KM), or Gaussian white noise random perturbations (EXP_WHITE) are run both for a linear convective-line of storms and a single "supercell" storm to demonstrate the utility of this new perturbation technique in diverse environments. PCSC perturbations are extracted from high-resolution simulations of boundary layer turbulence and the random perturbations are calibrated to be the same in magnitude as PCSC perturbations.

EXP_PCSC simulations spawn turbulence fastest in this study. The simulated turbulence is more robust than other experiments more than one hour into the simulation because horizontal convective rolls enhance power in the largest scales. Random

Abbreviations: IC, initial condition; PCSC, physically-coherent and spatially-correlated; QLCS, quasi-linear convective system; CAPE, convective available potential energy; RMSI, root mean square innovation; AGL, above ground level.

perturbations are slow to generate turbulence; this problem is exacerbated when the base model state flow is non-turbulent. Due to robust turbulence, EXP_PCSC ensemble spread increases fastest during the first simulation hour and remains largest throughout the remainder of the simulations. Although EXP_PCSC spread is largest, the sensitivity of convection to the initial perturbations varies at different times in the storm lifecycle. Storms appear more sensitive to perturbations added near the time of convective initiation.

KEYWORDS
Initial condition perturbations, ensemble spread, storm-scale forecasts, idealized simulations, turbulence

1 | INTRODUCTION

A challenge when creating an ensemble of storm-scale forecasts is to ensure initial condition (IC) perturbations accurately portray environmental variability that is typically not captured by observations. Creating optimal IC perturbations is especially important since small-scale errors can rapidly grow in amplitude and scale and impact the evolution of weather systems (Lorenz, 1969). Many idealized and real case studies demonstrate explicit forecasts of convection are sensitive to initial condition errors leading to changes in precipitation coverage, updraft area, and morphology (e.g., Zhang et al., 2006; Hohenegger and Schär, 2007; Zhang et al., 2016; Johnson and Wang, 2016; Potvin et al., 2017). Further, these errors can grow in scale and impact mesoscale and synoptic scale environments (e.g. Zhang et al., 2007). Aside from degrading forecast skill, incorrect estimates of IC uncertainty can cause convection-allowing forecast ensembles to become underdispersive (e.g., Clark et al., 2009, 2010; Romine et al., 2013; Flora et al., 2018; Loken et al., 2019) so that an observed event routinely occurs outside of the forecast probability density function. Given the sensitivity of convective forecasts to IC perturbations, extra attention is required to ensure the perturbations are optimal.

One of the most common techniques to generate an ensemble is to randomly perturb the forecast ICs (e.g., Snyder and Zhang, 2003; Zhang et al., 2004; Caya et al., 2005; Tong and Xue, 2005; Aksoy et al., 2009; Dowell et al., 2011; Sobash and Wicker, 2015). While easy to implement, there are many tunable parameters to consider when generating the perturbations such as amplitude and length scale. Experiments can also add IC perturbations to targeted regions of the experiment domain (e.g., near-storm regions) or certain model state variables to limit spurious convection (e.g., Snyder and Zhang, 2003) or spin-up of convection more quickly (e.g., Jung et al., 2012). Many studies select perturbations that enhance ensemble spread and limit spurious convection; however, they are typically unable to validate analysis uncertainity. Selecting more optimal IC perturbations remains elusive because extensive parameter tuning is required and their effectiveness is sensitive to the environment. To rely upon a less arbitrary selection process, novel strategies are being developed to calibrate IC perturbations.

Ideally, these new methods should attempt to calibrate ensemble perturbations to reflect sources of initial condition and forecast uncertainty. For example, Dawson et al. (2012) compared nearby velocity-azimuth display (VAD) observations within a low-level jet to understand local variations in wind speed and determine appropriate wind profile perturbations. While this method makes wind perturbations more representative of the observed environmental variability, the boundary layer is constantly evolving (e.g., Stull, 1988), which limits how appropriate these perturbations may be for other cases. Cintineo and Stensrud

(2013) used rapid update cycle (RUC) (Benjamin et al., 2004) forecast errors for multiple supercell cases to determine appropriate IC perturbations. Using forecast errors to constrain the perturbations provided important insights into the practical predictability of supercell thunderstorms at different forecast lead times. Both efforts to objectively calibrate IC perturbations are effective; however, their effectiveness remains dependent upon static parameters (e.g., amplitude, length scale, location) that are difficult to quantify and case sensitive.

Instead of defining optimal IC perturbations, Markowski (2020) simulates the upscale growth of modest potential temperature (θ) perturbations, which form different realizations of a steady-state boundary layer that serve as perturbed initial states. The turbulent eddies within the boundary layer are unique from typical random IC perturbations because they are physically coherent (i.e., all model state variables adjust to the impact of a perturbation) and spatially-correlated. Adding boundary layer turbulence to the initial conditions can impact fine-scale features such as near-surface vortices (Bryan et al., 2017; Markowski, 2020) and, to a lesser extent, the parent storm (Markowski, 2020). Although different realizations of a turbulent boundary layer have been used to evaluate the intrinsic predictability of severe weather events, no study has quantified the impact of these IC perturbations on ensemble spread. Due to the novelty of this approach, the benefit of physically-coherent and spatially-correlated (PCSC) perturbations over traditional ensemble perturbation methods (i.e., well-calibrated random perturbations) is unknown.

Most studies, especially idealized simulations initialized with horizontally homogeneous environments, continue to employ random perturbations to generate initial ensemble spread in part because few options are available. The goal of this study is to compare different IC perturbation techniques to determine which strategy increases ensemble spread most. Simulations initialized with PCSC perturbations and well-calibrated random perturbations are compared for a variety of cases. The results of this study provide an improved framework to initialize high-resolution simulations of convection.

The remainder of this study is as follows. Section 2 provides a brief description of two case studies used to test PCSC perturbations as well as the model settings and forecast evaluation metrics. A detailed description of how the IC perturbations are generated is presented in section 3 followed by experiment results in sections 4 and 5. The results are further discussed in section 6 along with concluding remarks and future research goals.

2 | EXPERIMENT DESCRIPTION

2.1 | Case Setup

Two idealized case studies are run to investigate how the IC perturbations impact high-resolution forecasts of convection. The same procedure is used to create the ensembles for each case study:

- Step 1: Use a sounding to initialize a single parent simulation.
- Step 2: Run the parent simulation at 1 km grid spacing for several hours.
- Step 3: Downscale the parent simulation to a 250 – m horizontal grid to produce a base model state (Fig. 2).
- Step 4: Add the IC perturbations to the base model state to create the high-resolution ensemble of simulations.
- Step 5: Run the high-resolution ensemble and evaluate the results.

The procedure used to create the high-resolution simulations resembles many previous studies. Forecasts of convection are commonly initialized with downscaled initial conditions (e.g., Johnson et al., 2015; Schwartz et al., 2015; Snook et al., 2016), and the effects of interpolation are minor because missing scales are recovered within the first 10-20 minutes of model integration (Potvin et al., 2017). The ensembles that are created are referenced by how they are initialized, either with PCSC perturbations (EXP_PCSC) or random perturbations (EXP_3KM, EXP_WHITE). A description of how the IC perturbations are created is detailed in section 3. The remainder of this subsection discusses how the parent simulation for each case is initialized.

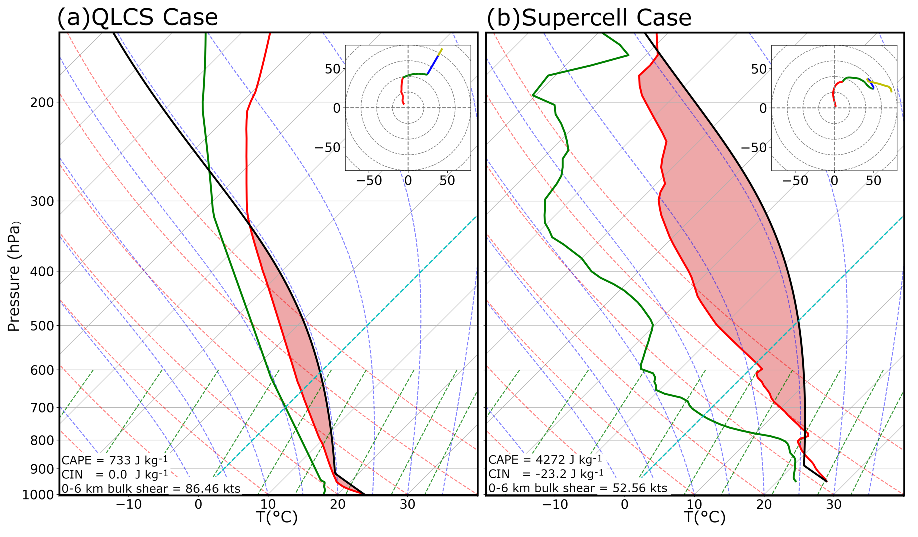

FIGURE 1 Soundings used to initialize the (a) QLCS and (b) supercell cases. In each sounding the solid red, green, and black lines correspond with the air temperature, dewpoint temperature, and temperature of an ascending surface-based parcel, respectively. Hodographs of wind speed (knots) are plotted in each upper right-hand corner. The hodograph color is based upon height above ground level (AGL) : 0 – 1 km is red, 1 – 3 km is green, 3 – 5 km is blue, 5 – 10 km is yellow.

The first case simulates the initiation and maintenance of a quasi-linear convective system (QLCS) that occurs in a strongly sheared (0 - 6 km bulk shear = 86.46 kts) and modestly unstable [convective available potential energy (CAPE) = 733 J kg^{-1}] environment. The Sherburn and Parker (2019) high-shear low-CAPE base-state sounding [Fig. 1a; generated via MetPy software (May et al., 2008)] initializes the horizontally homogeneous environment, though small modifications are made to lowest 100 mb of the sounding (e.g., increased near-surface lapse rate) to maintain boundary layer turbulence in the simulation. Following Sherburn and Parker (2019), a -10 K θ perturbation is inserted along the western edge of the domain to simulate a frontal boundary that provides the low-level forcing necessary to initiate convection. The perturbation decreases as a cosine function of the height above ground level (AGL) and distance from western boundary edge, and extends 260 km east of the domain boundary and 6 km above the surface. Modest (± 0.25 K) pseudorandom θ perturbations are also inserted in the environment, which results in a turbulent inflow region that is necessary to develop three-dimensional convective structures within the QLCS. These perturbations are distinct from the random or PCSC perturbations that generate the ensemble ICs, they grow in scale and cause the base model state environment to have weak turbulent motions (Fig. 2c). Downscaling (Step 3) occurs for the QLCS case when convection begins to initiate along the frontal boundary (Fig. 2a)

The second case is initialized with a highly unstable (CAPE > 4272 J kg^{-1}.) and strongly sheared (0 - 6 km bulk shear = 52.56 kts) environment that is supportive of supercell thunderstorms. The initial sounding (Fig. 1b) is extracted from a 24 May 2011 RUC analysis sampled near the supercell thunderstorm that produced an EF-5 tornado near El Reno, Oklahoma (Potvin and Flora, 2015). A 5 K warm-bubble that is 10 km wide and 1.5 km tall is inserted near the surface to initiate convection and form the supercell found in the case's base model state (Fig. 2b). Unlike the QLCS case, which requires small random θ perturbations inserted throughout the domain to generate three-dimensional structures, no initial random perturbations are added to the supercell case. Consequently, the inflow environment for this case is laminar (Fig. 2d), which is common for idealized experiments since many simulations of convection are initialized with horizontally homogeneous environments (Weisman and Klemp, 1982, 1984; Wicker and Wilhelmson, 1995; Adlerman et al., 1999; McCaul and Weisman, 2001). While running the

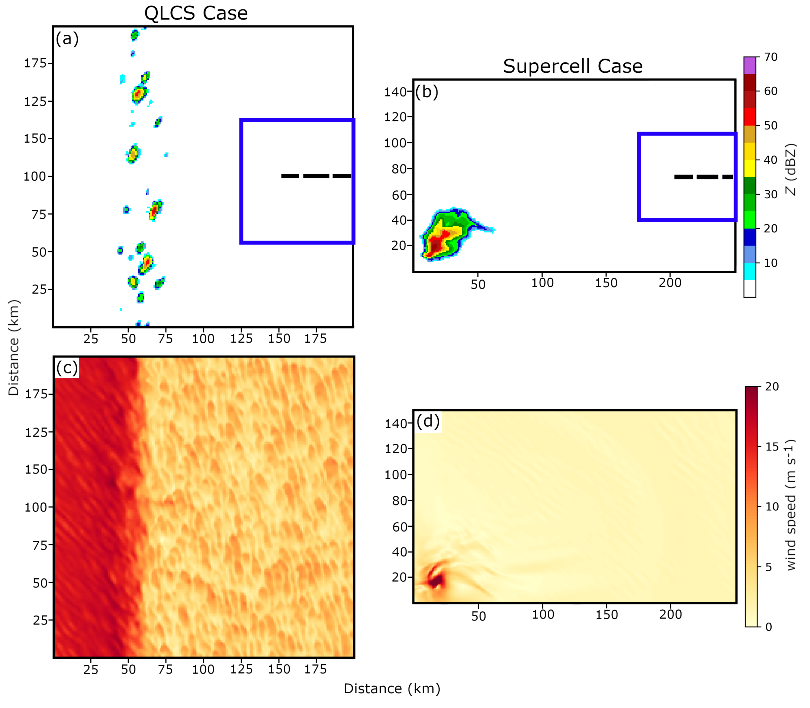

FIGURE 2 Base model state (a, b) reflectivity (*Z*) and (c, d) wind speed at the lowest model level for the (a, c) QLCS and (b, d) supercell cases when the ensembles are created. Blue squares mark the warm sector where one- and two-dimensional spectral densities are calculated (Fig. 4, 10) and black dashed lines mark where vertical cross-sections are sampled (Fig. 7, 13).

coarse parent simulation (Step 2), a supercell thunderstorm initiates and matures. Downscaling (Step 3) occurs when the supercell is robust (Fig. 2 b, d) and about to grow into a bowing line of storms.

2.2 | Prediction model settings

A brief summary of the prediction model settings is provided in Table 1. For each case, an ensemble of 36 simulations is run using a recent release (20) of the Cloud Model Version 1 (Bryan and Fritsch, 2002). The experiment configuration for both cases largely follows that of Sherburn and Parker (2019). Simulations are run at 250-m horizontal grid spacing and can resolve large-scale turbulent motions (Bryan et al., 2003). Coordinates are stretched in the vertical dimension with the finest vertical grid spacings located near the surface (Table 1). Both the vertical dimensions of the grid and the height at which Rayleigh damping is applied varies between cases to ensure the predicted convection remains within the domain. The supercell case assumes periodic lateral boundary conditions in all directions so that turbulent structures are maintained when crossing domain boundaries. The QLCS case assumes radiative east-west boundaries to maintain the cold temperature perturbation along the western boundary.

Subgrid-scale turbulence is parameterized using a variant of the Deardorff (1980) turbulent kinetic energy scheme. Coriolis acceleration only acts on perturbation winds, which is equivalent to assuming the base state wind field is in geostrophic balance (Roberts et al., 2016; Coffer et al., 2017; Sherburn and Parker, 2019). The National Severe Storms Laboratory (NSSL) double-moment microphysics scheme (Mansell et al., 2010) parameterizes precipitation processes. The scheme predicts six different hydrometeor categories including rain, cloud ice, cloud water, snow, graupel, and hail; both rimed ice categories also include

TABLE 1 Experiment settings for the evaluated case studies.

Parameter	QLCS Case	Supercell Case
Simulation duration	2 hours	2 hours
Domain dimensions	200 km × 200 km × 15 km	250 km × 150 km × 20.16 km
Vertical grid spacing	120 vertical levels 10 m at heights below 250 m 250 m at heights above 10 km	120 vertical levels 15 m at heights below 30 m 285 m at heights above 15.03 km
Rayleigh damping	Applied above 12 km	Applied above 18 km
Lateral boundary conditions	East-West: Radiative North-South: Periodic	East-West: Periodic North-South: Periodic
Horizontal grid spacing	250 m	
Bottom boundary condition	Free-Slip	
Microphysics	NSSL 2-moment (Mansell et al., 2010)	
Pressure solver	Klemp-Wilhelmson time-splitting, vertically implicit (Klemp and Wilhelmson, 1978)	
Subgrid turbulence	Turbulent Kinetic Energy (Deardorff, 1980)	

prognostic equations to update hydrometeor density.

Many of the modeling assumptions in this experiment are made for simplicity to focus on the impacts of the IC perturbations. Surface heat and moisture fluxes as well as radiative transfer are neglected, though it is noted that forecasts of convection are sensitive to radiative transfer (Markowski et al., 1998; Markowski and Harrington, 2005; Frame and Markowski, 2010, 2013; Nowotarski and Markowski, 2016). Like many previous idealized simulations of convective storms (e.g., Rotunno and Klemp, 1985; Wicker and Wilhelmson, 1995; Adlerman et al., 1999; Dahl et al., 2014; Sherburn and Parker, 2019), these experiments assume the bottom boundary condition is free-slip. Although the near-surface environment is sensitive to friction (e.g. Schenkman et al., 2012, 2014; Markowski, 2016; Roberts et al., 2016), parameterizing the impacts of surface friction remains a substantial challenge and can degrade the simulated wind profiles (Markowski and Bryan, 2016).

2.3 | Forecast evaluation

The IC perturbations generated during this study alter the state of the lower troposphere and cause storms to evolve differently amongst ensemble members. To this end, the first goal of this study is to identify how the simulated environment responds to IC perturbations. To isolate the perturbation impacts, the eastern portion of the experiment domain is evaluated (Fig. 2a - b). While this region of the domain is well ahead of the storm system at the time of analysis, it is representative of the larger environment that interacts with the storm system. This subdomain, which is referred to as the warm sector, was selected because it remains unaffected by convection until late in the simulation period.

Energy spectral distributions are often used to evaluate high-resolution simulations and understand how power is distributed across scales (e.g., Bryan et al., 2003; Skamarock, 2004; Gibbs and Fedorovich, 2014). One- and two-dimensional spectral density functions (spectra) evaluate the scale structure of the velocity field in the boundary layer (base model state + perturbations), which includes atmospheric structures both in the base model state field and the initial condition perturbations. For the v-component of velocity, which is evaluated during this study, x is defined as the transverse direction with a corresponding wavenumber (k_1) of $2\pi/\lambda_x$ and y is defined as the longitudinal direction with a corresponding wavenumber (k_2) of $2\pi/\lambda_y$. λ_x and λ_y are wavelengths in the respective x and y directions. One-dimensional spectra are calculated along each row of the warm sector region in the y-direction and averaged in the x-direction (Kaiser and Fedorovich, 1998). Two-dimensional spectral density plots are calculated via a planar Fourier transform (Kelly and Wyngaard, 2006).

Observation-space diagnostic statistics including the root-mean square innovation (RMSI) and ensemble spread evaluate how the IC perturbations impact convection. Given that these experiments are idealized, there are no real-case observations available. Instead, simulated observations for each case study are extracted from a simulation initialized from the unperturbed base model state. The simulation initialized from the unperturbed base model state is not the same as the ensemble mean because convection responds non-linearly to the turbulence. Thus, the mean of simulations diverges from the observations during the simulation. The RMSI is defined as

$$RMSI = \sqrt{\langle d^2 \rangle}, \tag{1}$$

where d (the innovation) is the difference between an observation (y^0) and the model state mapped to observational space via a forward operator [H(x^f)]:

$$d = y^0 - \overline{H(x^f)}, \tag{2}$$

$\langle d \rangle$ is the innovation averaged over all observations, and $\overline{H(x^f)}$ is the ensemble mean of the model state mapped to observation space. The ensemble spread (Dowell and Wicker, 2009) is defined as:

$$spread = \sqrt{\langle \frac{1}{N-1} \sum_{n=1}^{N} [H(x_n^f) - \overline{H(x^f)}]^2 \rangle}, \tag{3}$$

where N is the ensemble size. Given the idealized nature of this study the observation error variance is ignored. Statistics are only considered where the observed or the ensemble mean reflectivity (Z) exceeds 15 dBZ. Radar reflectivity is diagnosed from model output using the NSSL microphysical parameterization radar forward operator. This operator employs the Rayleigh scattering approximation to calculate the scattering amplitudes for precipitating hydrometeor types (rain, snow, graupel, hail, cloud ice).

Another useful observation-space statistic evaluated during this study is the consistency ratio (Dowell et al., 2004; Dowell and Wicker, 2009; Aksoy et al., 2009; Yussouf et al., 2013; Potvin et al., 2013). This ratio is defined as:

$$consistency\ ratio = \frac{\langle \frac{1}{N-1} \sum_{n=1}^{N} [H(x_n^f) - \overline{H(x^f)}]^2 \rangle}{\langle d^2 \rangle}. \tag{4}$$

Ensemble variance is considered to be a good approximation of the forecast error variance when the consistency ratio is approximately one, but the ensemble becomes overdispersive (underdispersive) when the ratio substantially increases (decreases) from one.

3 | DESCRIPTION OF PERTURBATION METHODOLOGY

A flowchart (Fig. 3) is provided to detail how to the IC perturbations are created and initialize ensembles of high-resolution simulations. Following a similar methodology to Markowski (2020), 36 simulations of boundary layer turbulence are run for each case to generate the IC perturbations. Simulations of boundary layer turbulence are run with the same prediction model settings as the simulations they perturb (Table 1), except that all boundary layer turbulence simulations are run with doubly periodic lateral boundary conditions. Case soundings initialize the environment. For each ensemble member, a different set of pseudorandom θ perturbations (± 0.25 K) are inserted throughout the domain. These perturbations are uncorrelated between

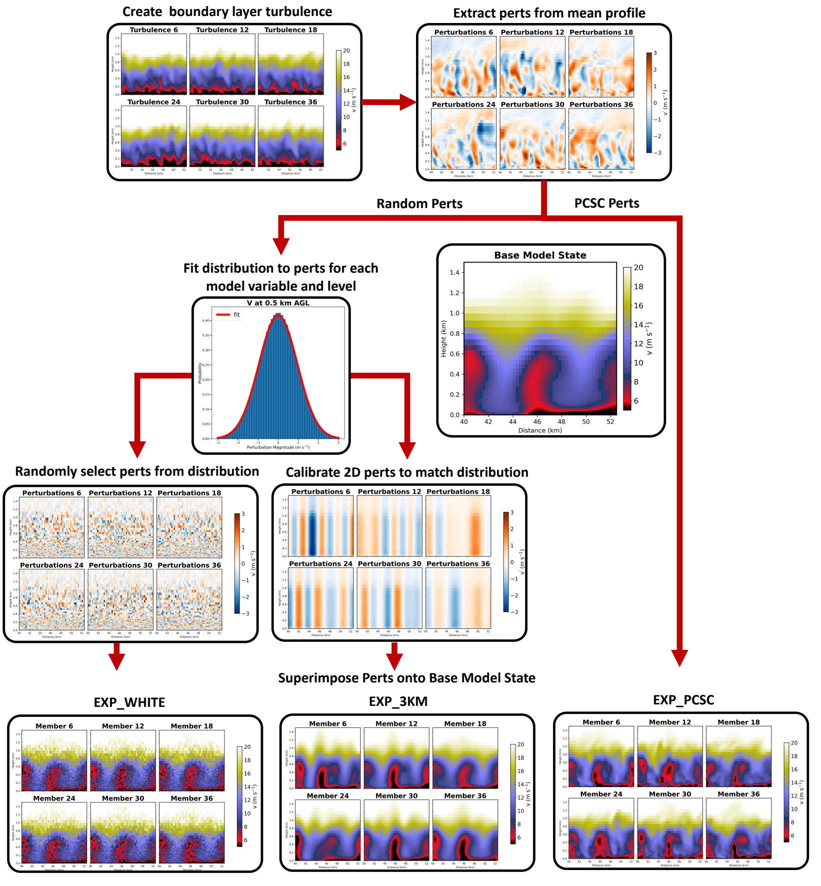

FIGURE 3 A flowchart diagraming how white noise (left-most column), 3 km (center column), and PCSC (right-most column) perturbations are generated and initialize ensembles of high-resolution simulations. Vertical cross-sections are taken from within the warm sector of the QLCS case (Fig. 1a).

adjoining grid points and are akin to white noise. The simulations are run for 12 hours, during which the initial perturbations grow in scale to form different realizations of a turbulent boundary layer. Although the simulated turbulence evolves differently with time, the domain average profile is identical between simulations for each case.

The difference between model state variables and the domain average profile is calculated at each grid point to extract perturbations for dynamic state variables (i.e., u, v, w), water vapor mixing ratio (q_v), and θ. Hydrometeor fields are not perturbed during this study, thermodynamic and moisture perturbations cause precipitation fields to evolve differently as the simulations are integrated forward in time. The extracted perturbations average to 0 across the domain. Mean absolute perturbations are largest where boundary layer turbulence is prevalent (approximately 0 - 3 km AGL) and decrease further aloft. The complex nature of these extracted perturbations highlights the challenge of creating IC perturbations that match environmental variability. The remainder of this section describes how PCSC and random perturbations are created.

3.1 | PCSC perturbations

To initialize an EXP_PCSC ensemble member, perturbations extracted from each boundary layer turbulence simulation is superimposed either onto the supercell or QLCS base model state. This process is repeated 36 times, creating the initial ensemble for either case. Since turbulence simulations are run for both the QLCS and supercell cases, the PCSC perturbations are tailored to the environment of each case.

Vertical cross-sections taken within the QLCS warm sector demonstrate how PCSC perturbations impact the environment. The downscaled base model state (Fig. 3) contains relatively weak and smoothed vertical motions. Since boundary layer turbulence simulations are run for 12 hours at finer grid spacings, the PCSC v perturbations resolve smaller features and are often more intense than the base model state (Fig. 3 upper-right). Superimposing PCSC perturbations onto the base model state (Fig. 3 bottom-right) causes new atmospheric structures to develop and increases ensemble diversity.

3.2 | Random perturbations

Two types of random perturbations (EXP_3KM, EXP_WHITE) are generated during this study, both represent different types of perturbations employed by recent studies. Many data assimilation experiments apply smoothed random perturbations (e.g., Caya et al., 2005; Dowell and Wicker, 2009; Jung et al., 2012; Sobash and Stensrud, 2013) to the initial model field to generate ensemble spread. To replicate these perturbations, this study creates random two-dimensional perturbations that are 3 km in scale using an analytical approach introduced in Bryan et al. (2007). To add vertical depth, the perturbations are repeated over each model level. The 3 km perturbations are tuned so that standard deviation of the 3 km perturbations matches that of the PCSC perturbations for each model level and model state variable (i.e., u, v, w, q_v, θ). Similar strategies are employed in previous studies, which apply a Gaussian filter to two-dimensional perturbations to add vertical depth (e.g., Jung et al., 2012). Finally, the 3 km perturbations are superimposed onto the base model state for each respective case to create EXP_3KM ensemble members.

Modeling studies often insert random perturbations that are spatially small in either the horizontal or vertical direction (e.g. Dawson et al., 2012; Coffer and Parker, 2017; Sherburn and Parker, 2019; Flournoy et al., 2020) to account for observational error and sampling inconsistencies. This technique is performed under the assumption that small-scale errors grow rapidly in scale and impact the broad environment and storm evolution (e.g., Lorenz, 1969). To replicate these perturbations, this study randomly draws perturbations for each model state variable at each model level from the corresponding distribution of PCSC perturbations. Doing so causes the distribution of PCSC and white noise perturbations to become nearly identical. The perturbations, which initialized EXP_WHITE ensemble members, are Gaussian white noise and thus change substantially between adjacent grid points. Unlike PCSC perturbations which change the structure of the environment when superimposed onto the base model state, the EXP_WHITE perturbations increase initial condition variance at small scales (Fig. 3 bottom-left).

4 | QLCS RESULTS

4.1 | Simulated Turbulence

One-dimensional spectral density functions (1D Spectra) of the v-component of velocity (P_v) are sampled at 0.5 km AGL in the warm sector (Fig. 4a) to assess how IC perturbations impact the scale-dependent properties of the environment. The EXP_PCSC spectrum at initialization (Fig. 4a) follows the -5/3 power law (Kolmogorov, 1941) at scales larger than the approximate effective resolution (approximately 6Δx or 1.5 km), which suggests the simulations resolve the cascade of energy from large to small turbulent eddies in the inertial subrange. This is consistent with Bryan et al. (2003), which showed simulations must be run at horizontal grid spacings of 250 m or less to resolve the inertial subrange. The corresponding EXP_3KM and EXP_WHITE

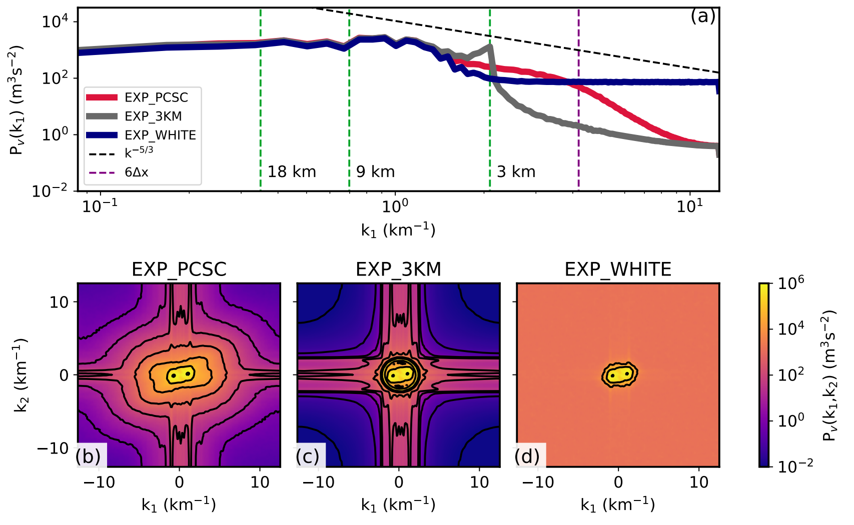

FIGURE 4 (a) A one-dimensional spectral density plot of the *v*-component of velocity (base model state + perturbations) sampled 0.5 km AGL in the QLCS warm sector at initialization. Plotted spectra are averaged across ensemble members for EXP_PCSC (red), EXP_3KM (grey), and EXP_WHITE (blue). The dashed black line is the -5/3 power law, the vertical dashed purple line marks the approximate effective resolution, and the vertical dashed green lines are the wavelengths over which spectral density time series are evaluated (Fig. 6). (b - d) Two-dimensional spectral density plots averaged across ensemble members at initialization. Contours represent spectral density in powers of 10.

spectra (Fig. 4a) are unable to replicate the energy cascade. This is because the analytic function used to create the 3 km perturbations acts as a low pass filter to remove small scale features and the white noise perturbations add equal power to all scales. Although random perturbation spectra slowly evolve to become more realistic with time, the initial model state is inconsistent with turbulence theory.

PCSC perturbations represent coherent atmospheric structures that cause robust turbulence to quickly form in simulations. The EXP_PCSC 1D spectrum consequently has more power than EXP_WHITE at scales larger than the effective resolution (Fig. 4a) at initialization. In comparison, the EXP_3KM spectrum has enhanced power at 3 km, the initial horizontal scale of the random perturbations, but has limited power at all smaller scales. Spectra from all three experiments have increased power at larger scales ($k_1 < 10^0$ km^{-1}) because perturbations are superimposed on the QLCS base model state, which contains weak turbulent structures in the warm sector (Fig. 5). While the spectra appear similar at these scales because spectral density is plotted on a logarithmic scale, EXP_PCSC has considerably more power at scales exceeding 10 km in length because the PCSC perturbations contain horizontal convective rolls that span many kilometers (Fig. 5a).

Two-dimensional spectral density functions (2D Spectra; Fig. 4b-d) also evaluate differences in scale dependencies between ensembles at initialization. The 2D spectra are plotted as a function of wavenumber both in the transverse (k_1) and longitudinal directions (k_2); large scales are plotted in the center and small scales are plotted on the outer periphery. The stark contrast between EXP_PCSC 2D spectrum (Fig. 4b) and the other ensembles (Fig. 4c-d) highlights the challenge of generating IC perturbations that are representative of atmospheric phenomena. The EXP_PCSC 2D spectral density contours (Fig. 4b) are compressed towards large scales and elongated in the transverse direction. This is consistent with turbulence theory because the ratio of transverse to longitudinal spectra in the inertial subrange should exceed one (Tennekes and Lumley, 1972). While the EXP_PCSC spectrum (Fig. 4b) is representative of boundary layer turbulence, the EXP_WHITE 2D spectrum (Fig. 4d)

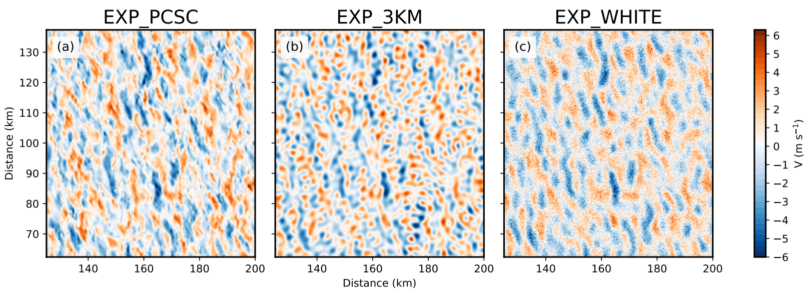

FIGURE 5 The deviation of v-component of velocity (base model state + perturbations) from the mean environment at 0.5 km AGL in the QLCS warm sector (Fig. 2a). Plots highlight the weak turbulent eddies in the base model state and the superimposed initial condition perturbations. The first ensemble member of (a) EXP_PCSC, (b) EXP_3KM, and (c) EXP_WHITE at initialization is plotted.

is not. This is because the random perturbations add constant power in all directions and cause the spectral density to remain constant at most scales. The EXP_3KM spectrum (Fig. 4c) is also inconsistent because the spectral density is compressed in a narrow band approximately 3 km in wavelength and equally distributed in the longitudinal and transverse directions. Although EXP_WHITE and EXP_3KM spectral densities are initially different in structure, they slowly evolve to resemble EXP_PCSC because boundary layer turbulence builds in the simulations.

Although each experiment is different at forecast initialization, the power spectra evolve to become more similar with time. To determine how long ensemble differences remain, a time series of 1D spectra sampled at wavelengths of 3 km, 9 km, and 18 km (Fig. 6) tracks the evolution of the environment. The time series (Fig. 6) demonstrate that experiment differences are largest during the first 10 – 20 minutes of the QLCS simulation period. During this time the EXP_PSCSC spectrum has enhanced power scales between 9 and 18 km (Fig. 6b, c). The EXP_3KM 1D spectrum initially has enhanced power at 3 km in scale (Fig. 6a), though this is short lived because the IC perturbations change in scale and structure. After a brief spin-up period, the spectra for all three experiments become relatively similar at scales between 3 and 9 km (Fig. 6a, b), though the EXP_PCSC 1D spectrum has more power at larger scales (Fig. 6c). These differences have the potential to impact evolution of the QLCS.

Vertical cross-sections taken through the warm sector (Fig. 7) show the variance of v is confined to the boundary layer and rapidly decreases further aloft. The atmosphere above the boundary layer is typically more stable (Stull, 1988), which limits the vertical extent of turbulence and suppresses ensemble variance. EXP_3KM and EXP_WHITE capture this variance gradient (Fig. 7b, c) because the perturbations are calibrated using simulations of boundary layer turbulence; however, tuning random perturbations with no reference solution would pose a challenge. Ensemble variance is largest during the first 30 minutes (Fig. 7a - c) when turbulence is strong because the simulations adjust to the new IC perturbations. As the simulated environment becomes more balanced and turbulence moderates, variance slowly decreases with time (Fig. 7d-f)

PCSC perturbations cause simulations to develop robust turbulence fast, which enhances the variance of v in the boundary layer. Consequently, the variance of EXP_PCSC predicted v at 30 minutes (Fig. 7a) is considerably larger than EXP_WHITE (Fig. 7c) and, to a lesser extent, EXP_3KM (Fig. 7b). At this time the EXP_PCSC turbulence is more intense, which not only enhances velocity variance, but also increases spectral density at large scales (Fig. 6c). Ensemble differences diminish with time as the simulations adjust to the IC perturbations; however, the effects of the initial perturbations are long lasting and EXP_PCSC variance consistently remains the largest.

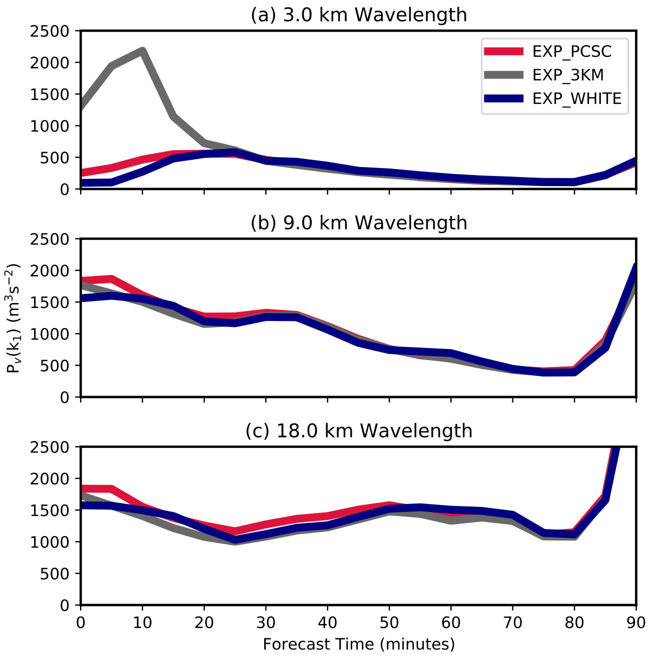

FIGURE 6 A time series of the 1D ensemble average spectra sampled at horizontal scales of (a) 3 km, (b) 9 km, and (c) 18 km during the first 90-minutes of the QLCS simulation. Spectra are of the *v*-component of wind sampled at 0.5 km AGL. Red, grey, and blue lines correspond with EXP_PCSC, EXP_3KM, and EXP_WHITE, respectively.

4.2 | Storm Spread

The ensemble spread and RMSI of in-storm fields analyzes (Fig. 8) how IC perturbations impact the evolution of the QLCS. Ensemble spread and RMSI increase fastest during the first hour of the simulation, when the variance of *v* is largest due to the presence of robust turbulence (Fig. 7a-c). Enhanced turbulence alters low-level moisture, temperature, and wind perturbations that impact convective evolution (e.g., Crook, 1996), and consequently accelerates growth of ensemble spread. Error growth slows after the first hour (Fig. 8), coinciding with when the initial turbulence moderates and causes velocity variance to decrease.

Although all ensembles exhibit similar trends in error growth, forecast RMSI and spread is typically largest for the EXP_PCSC simulations (Fig. 8). EXP_PCSC forecast error is enhanced because the IC perturbations quickly spawn robust turbulence that has enhanced power at larger scales (Fig. 6c). The turbulent eddies cause the QLCS to evolve differently amongst ensemble members because forecasts of convection are sensitive to modest changes in the environment (e.g., Zhang et al., 2006; Hohenegger and Schär, 2007; Potvin et al., 2017). EXP_3KM IC perturbations also increase the variance of *v* (Fig. 7b, e) and cause RMSI values to become nearly as large. EXP_WHITE velocity variance is weakest and consequently the ensemble innovations and spread are smallest. Despite RMSI differences, consistency ratios for all three ensembles are comparable in part because ensemble spread remains a good approximation of the forecast error variance (e.g., Dowell and Wicker, 2009).

Supporting the results of domain average statistics (e.g., ensemble spread), the variance of EXP_PCSC predicted rainwater mixing ratio (q_r) at the lowest model level remains largest throughout the simulation (Fig. 9). The variance of EXP_PCSC q_r is largest in magnitude early in the simulation (Fig. 9a) because the predicted convection interacts with robust turbulence that alters predicted rainfall intensity and location. Although the experiments appear more similar at later times (Fig. 9d-f), the areal

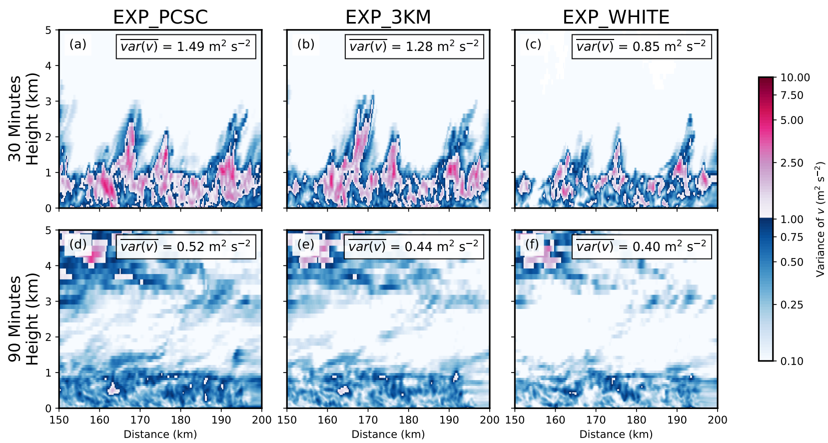

FIGURE 7 Vertical cross-sections showing the ensemble variance of the v-component of velocity in the QLCS warm sector (Fig. 2a) for (a, d) EXP_PCSC, (b, e) EXP_3KM, and (c, f) EXP_WHITE. The average variance of v sampled at 0.5 km AGL in the warm sector is listed in the upper right-hand corner of each plot.

coverage of grid points exceeding a high variance threshold (var(q_r) > 1.00 g ^{2} kg^{-2}) remains considerably larger for EXP_PCSC than EXP_WHITE. The areal coverage of enhanced rainfall variance increases in EXP_3KM (Fig. 9e) simulations but remains smaller than EXP_PCSC (Fig. 9d). PCSC perturbations enhance wind variance in the warm sector throughout the simulation (Fig. 7a, d), which given the sensitivity of convection to modest uncertainties (e.g., Zhang et al., 2015), increases precipitation variance (Fig. 9a, d). The rapid spin-up and maintenance of EXP_PCSC ensemble spread is attributed to the physically coherent IC perturbations.

5 | SUPERCELL RESULTS

5.1 | Simulated Turbulence

Turbulence differences between experiments are more prominent for the supercell case because, unlike the prior case, the base model state flow is laminar in regions unimpacted by convection (Fig. 2d). The EXP_WHITE 1D (Fig. 10a) and 2D (Fig. 10d) spectra at initialization are constant in power at all scales because the random perturbations act similar to white noise. Unlike the prior case, EXP_WHITE spectral density does not increase at larger scales because the base model state contains no turbulence and the perturbations are small in scale (Fig. 11c). Given the uniform size of 3 km perturbations (Fig. 11b), EXP_3KM 1D (Fig. 10a) and 2D (Fig. 10c) spectral densities are compressed at 3 km in scale and decrease with any change in scale. The EXP_PCSC 1D spectrum (Fig. 10a) has enhanced power at all scales exceeding the approximate effective resolution (i.e., 1.5 km) because the PCSC perturbations contain horizontal convective rolls (Fig. 11a) that develop in strongly sheared and unstable environments (e.g., Brown, 1970). The spectrum also follows the -5/3 power law (Kolmogorov, 1941) at scales larger than the effective resolution (Fig. 10a), which suggests the simulations resolve the inertial subrange. Consistent with the QLCS case and turbulence theory (Tennekes and Lumley, 1972), EXP_PCSC 2D spectral densities (Fig. 10b) are compressed towards larger scales and elongated in the transverse direction.

Time series of the spectral density functions sampled at various scales demonstrate that the EXP_PCSC 1D spectrum has increased power at large scales (e.g., 18 km) during most the simulation (Fig. 12c). This is because the IC perturbations spawn

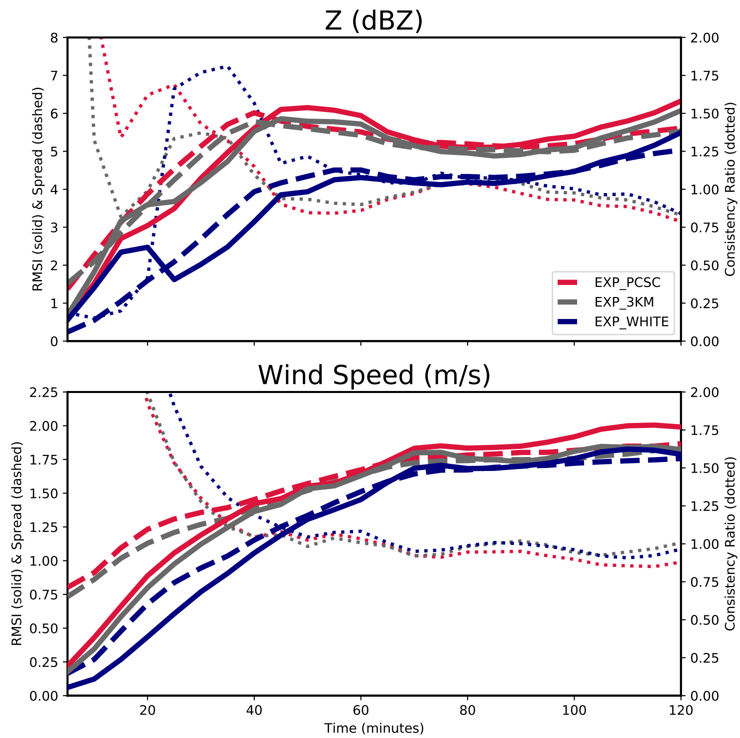

FIGURE 8 The RMSI (solid line) and ensemble spread (dashed lined) of (a) Z and (b) wind speed sampled at 0.5 km AGL for the QLCS case. Statistics are considered where observations or ensemble mean Z exceed 15 dBZ. Consistency ratios (dotted line) are plotted on the secondary (right-hand) axis. Red, grey, and blue lines correspond with EXP_PCSC, EXP_3KM, and EXP_WHITE, respectively.

horizontal convective rolls (Fig. 11a) that span many kilometers and increase spectral density in the mesoscale. EXP_WHITE turbulence remains weak at the beginning of the simulation and consequently the corresponding 1D spectrum has less power than EXP_PCSC at all evaluated scales 30 minutes into the simulation (Fig. 12). Although missing scales can be generated shortly after forecast initialization (e.g. Potvin et al., 2017), additional time is required to generate turbulence when random incoherent perturbations are inserted in a laminar flow. EXP_3KM perturbations substantially increase spectral density at 3 km in scale (Fig. 12a); however, much of this energy is lost as the perturbations evolve. EXP_3KM is also unable to simulate the growth of robust large-scale perturbations. Consequently, the ensemble has the least power at scales exceeding 9 km (Fig. 12b, c) throughout the simulation. Results suggest the smoothed 3 km perturbations grow in scale much slower when superimposed on a laminar flow environment.

The variance of EXP_PCSC predicted v remains enhanced in the boundary layer throughout the simulation (Fig. 13). EXP_PCSC turbulence has more power than EXP_3KM and EXP_WHITE at most evaluated scales (Fig. 12), which increases wind variance (Fig. 13a). The variance of EXP_3KM v is initially large because the IC perturbations substantially increase power at small scales (Fig. 12a); however, variance decreases because the perturbations weaken. Although slow to generate turbulence, EXP_WHITE wind variance slowly increases with time (Fig. 13c, f) and exceeds EXP_3KM during the first simulation hour. This is because large turbulent eddies simulated in the former ensemble become more robust and increase spectral density at all

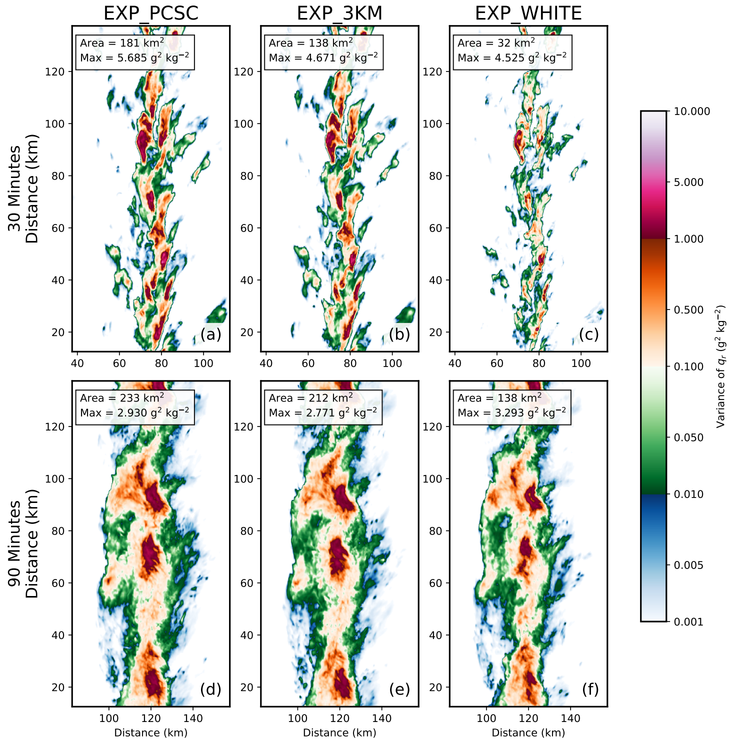

FIGURE 9 The ensemble variance of q_r at the lowest model level above the surface for (a, d) EXP_PCSC, (b, e) EXP_3KM, and (e, f) EXP_WHITE for the QLCS case. Tables in the upper left-hand corner of each plot show areal coverage of grid points exceeding a high variance threshold (var(q_r) > 1.00 g^2 kg^{-2}) and maximum variance. Plots are centered upon the location of convection.

evaluated scales (Fig. 12).

5.2 | Storm Spread

EXP_3KM has the largest RMSI values for both Z and wind speed (Fig. 14) during the simulation period in part because the initially robust small-scale perturbations temporarily enhance wind variance (Fig. 13b). Although EXP_3KM innovations are large, the ensemble spread increases at a much slower rate (Fig. 14) and causes the ensemble to become spread deficient ($0.5 <$ consistency ratio < 0.7). This is consistent with previous studies, which note incorrect estimates of IC uncertainty can cause convection-allowing forecast ensembles to become underdispersive (e.g., Clark et al., 2009, 2010; Romine et al., 2013; Flora et al., 2018; Loken et al., 2019). EXP_PCSC and EXP_WHITE Z simulations are also spread deficient, though to a lesser extent (consistency ratio ≈ 0.75). Although the consistency ratio is often less than unity, EXP_PCSC ensemble spread is larger than any other experiment throughout the simulation, which causes the ensemble to have the largest consistency ratio values (Fig. 14).

EXP_PCSC q_r variance is larger than both EXP_3KM and EXP_WHITE throughout the simulation (Fig. 15) because robust turbulence alters precipitation intensity, location, and areal coverage. Unlike the previous case, EXP_3KM predicts the smallest areal coverage of high rainfall variance (i.e., $q_r > 1.0$ g^2 kg^{-2}) because the IC perturbations are slow to grow in scale.

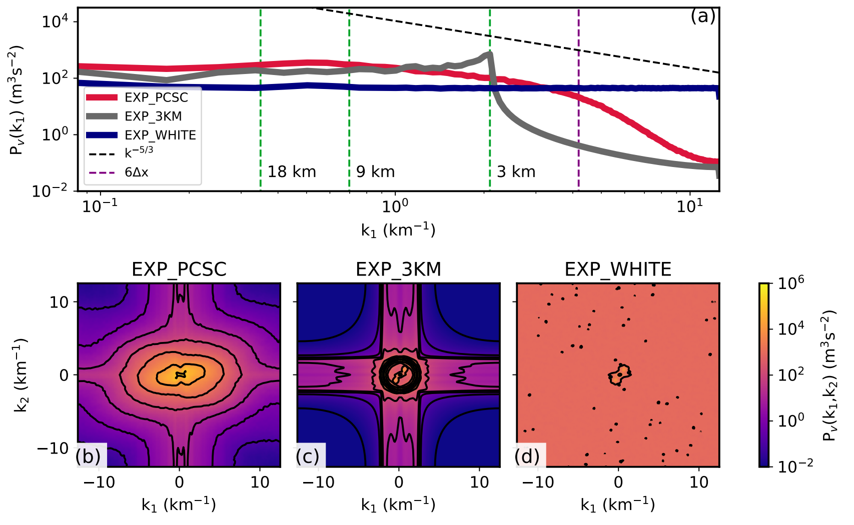

FIGURE 10 (a) A one-dimensional spectral density plot of the v-component of velocity (base model state + perturbations) sampled 0.5 km AGL in the supercell warm sector at initialization. Plotted spectra are averaged across ensemble members for EXP_PCSC (red), EXP_3KM (grey), and EXP_WHITE (blue). The dashed black line is the -5/3 power law, the vertical dashed purple line marks the approximate effective resolution, and the vertical dashed green lines are the wavelengths over which spectral density time series are evaluated (Fig. 12). (b - d) Two-dimensional spectral density plots averaged across ensemble members at initialization. Contours represent spectral density in powers of 10.

The areal coverage of high rainfall variance is modestly larger for EXP_WHITE because the perturbations become robust at larger scales and thus have a greater impact storm evolution. For lower q_r variance thresholds (i.e., > 0.01 g^2 kg^{-2}, > 0.1 g^2 kg^{-2}) , EXP_3KM and EXP_WHITE perform similarly early in the forecast period. EXP_3KM predicts the smallest areal coverage for all evaluated thresholds at later times. Although all three ensembles eventually predict a large swath of enhanced rainfall variance (Fig. 15 d-f), the maximum variance during the first 30 minutes of the supercell case (Fig. 15a-c) is much lower than the QLCS case (Fig. 9a-c). Results highlight that storm response to turbulence is case dependent.

Forecast uncertainty is often impacted and potentially dominated by atmospheric interactions that occur near the time of convective initiation, including horizontal convective rolls converging upon air mass boundaries (e.g., Wilson et al., 1992; Martin and Xue, 2006; Weckwerth et al., 2008) and the initiation and subsequent merger of multiple storms (e.g., Wurman et al., 2007; Skinner et al., 2014; Tanamachi et al., 2015; Hastings and Richardson, 2016; Klees et al., 2016). Unlike the QLCS case, which is initialized during initiation (Fig. 2a), this case is initialized with a mature supercell thunderstorm (Fig. 2b), and consequently the turbulence does not necessarily have a proportionate impact on convection. However, once the supercell thunderstorm transitions into a bowing line of storms, the ensemble rainfall variance increases considerably. Interactions between convection and the turbulent environment are complex and the subsequent evolution of storms is highly non-linear. To ensure forecast uncertainty is optimally represented it appears important to generate realistic ensemble perturbations quickly so they are present throughout the duration of a convective system.

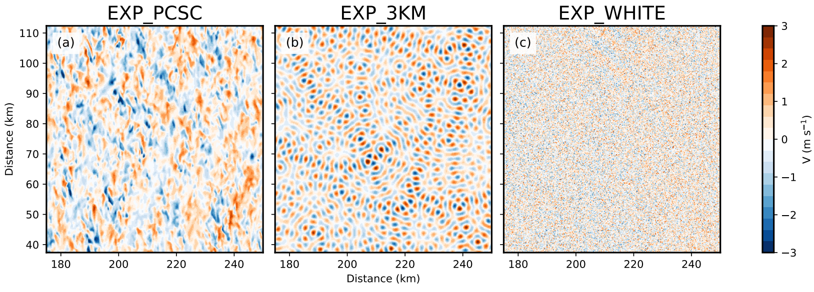

FIGURE 11 The deviation of v-component of velocity from the mean environment at 0.5 km AGL in the supercell warm sector (Fig. 2b). The first ensemble member of (a) EXP_PCSC, (b) EXP_3KM, and (c) EXP_WHITE at initialization is plotted.

6 | CONCLUSIONS

This study expands upon Markowski (2020) and introduces a novel technique to generate storm-scale perturbations that are both physically-coherent and spatially-correlated (PCSC) and require little calibration once generated. To create these perturbations, an ensemble of high-resolution simulations (Δx = 250 m) initialized with modest and random potential temperature perturbations is run for 12 hours to generate different realizations of a turbulent boundary layer. Each realization provides a unique set of initial condition (IC) perturbations used to generate an ensemble of high-resolution simulations of convection.

Ensembles initialized either via PCSC perturbations (EXP_PCSC) or random perturbations (EXP_3KM, EXP_WHITE) are compared. To create the EXP_3KM ensemble, random perturbations that are 3 km in scale in the horizontal are superimposed onto the base model state. These perturbations are designed to resemble smoothed random perturbations employed in data assimilation experiments (e.g., Caya et al., 2005; Dowell and Wicker, 2009; Jung et al., 2012; Sobash and Stensrud, 2013) to increase ensemble spread. To create the EXP_WHITE ensemble, Gaussian white noise is superimposed onto the base model state. Many idealized modeling studies (e.g. Dawson et al., 2012; Coffer and Parker, 2017; Sherburn and Parker, 2019; Flournoy et al., 2020) rely upon small-scale perturbations to generate spread under the assumption that the perturbations quickly grow in scale and impact the evolution of convection. The random perturbations in both ensembles are calibrated so that the distribution of the perturbation magnitudes matches the PCSC perturbations for each model level and perturbed variable (i.e., u, v, w, q_v, θ). Ensembles are run for two idealized cases to determine the feasibility of employing PCSC perturbations in diverse environmental conditions. The first set of ensembles simulate a quasi-linear convective system (QLCS) that initiates along a frontal boundary in a highly-sheared and modestly-unstable environment. The second set of ensembles simulate a supercell thunderstorm that grows into a bowing line of storms in a highly-sheared and highly-unstable environment. These experiments are used to understand how the different types of IC perturbations impact ensemble spread and the predicted evolution of convection

The warm sector environment ahead of the approaching convection is analyzed to understand how the simulated environment responds to the IC perturbations. Spectral density analyses reveal the Gaussian white noise perturbations add constant power to all scales, while the 3 km perturbations increase power most over a narrow band of wavelengths (i.e, 3 km). Both types of random perturbations are slow to generate robust turbulence, a problem that is exacerbated for the supercell case because the base model state contains no turbulent eddies in the warm sector. Simulations initialized with PCSC perturbations quickly spawn horizontal convective roles that enhance spectral density in the mesoscale. Due to the enhanced and mature turbulent structures, EXP_PCSC simulations generally have more power than EXP_3KM and EXP_WHITE at scales exceeding 10 km more than one hour into the simulation. This causes EXP_PCSC wind variance in the boundary layer to be larger than both EXP_3KM and EXP_WHITE throughout the simulation.

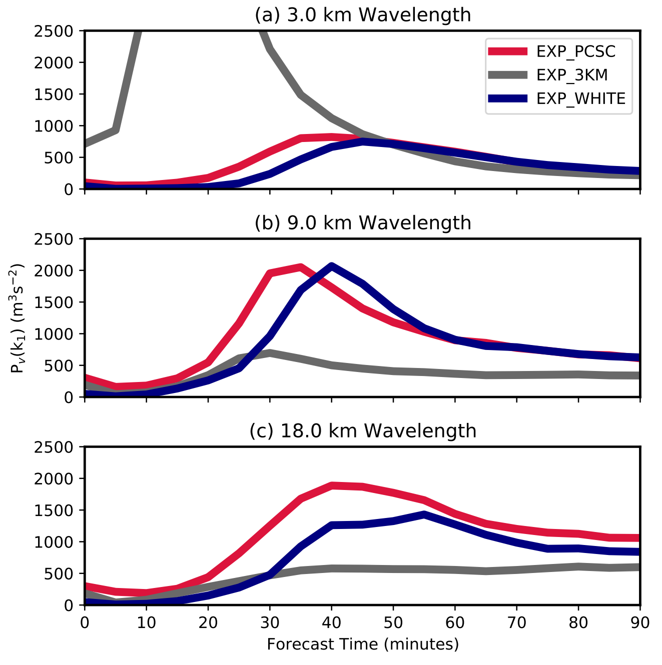

FIGURE 12 A time series of the 1D ensemble average spectra sampled at horizontal scales of (a) 3 km, (b) 9 km, and (c) 18 km during the first 90-minutes of the supercell simulation. Spectra are of the *v*-component of wind sampled at 0.5 km AGL. Red, grey, and blue lines correspond with EXP_PCSC, EXP_3KM, and EXP_WHITE, respectively.

EXP_PCSC storm spread is enhanced (i.e., convection is more diverse) in both cases because the predicted storms interact with robust boundary layer turbulence spawned by IC perturbations. The turbulent eddies in the EXP_PCSC simulations quickly create and maintain physically coherent perturbations that grow in scale and alter the evolution of convective storms. Results concur with previous studies that note high-resolution forecasts are initially sensitive to the upscale growth of small-scale initial perturbations (e.g., Zhang et al., 2006, 2016; Potvin et al., 2017). Since the random perturbations are initially slow to develop robust mesoscale structures, the ensemble storm spread increases at a slower rate initially. The more rapid spin-up of EXP_PCSC spread increases forecast uncertainty and potentially mitigates ensemble underdispersion, a well-documented problem for convection-allowing forecast ensembles (e.g. Clark et al., 2010; Romine et al., 2014; Loken et al., 2019).

Storm sensitivity to boundary layer turbulence varies between the QLCS and Supercell cases. Although perturbations are generated using the same techniques for both storm events, the variance of q_r for the supercell case is initially much smaller than the QLCS case. Rainfall variance is hypothesized to be initially larger for the QLCS case because the IC perturbations are added during convective initiation, rather than when the supercell is fully mature. However, once the supercell grows in scale and form a bowing line of storms, ensemble variance of of q_r grows considerably faster. Forecast error is often impacted by atmospheric interactions that occur near the time of convective initiation (e.g., Wilson et al., 1992; Martin and Xue, 2006; Weckwerth et al., 2008), which can alter the impact of turbulence on predicted convection. Further, changes in storm mode and the environment alters forecast uncertainty (e.g., Lawson, 2019). Results highlight the importance of quickly generating realistic ensemble perturbations that are present throughout the lifecycle of a storm. While determining when convection is most sensitive to IC perturbations is beyond the scope of this study, the novel perturbation framework can be extended in future cases to better

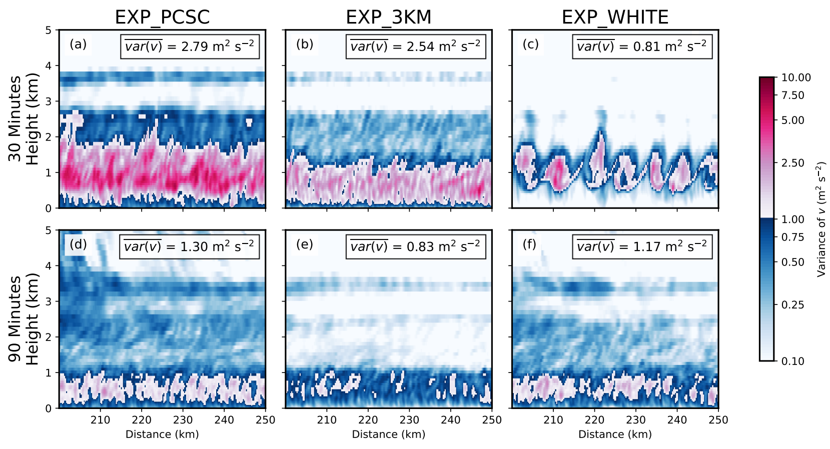

FIGURE 13 Vertical cross-sections showing the ensemble variance of the v-component of velocity in the supercell warm sector (Fig. 2b) for (a, d) EXP_PCSC, (b, e) EXP_3KM, and (c, f) EXP_WHITE. The average variance of v sampled at 0.5 km AGL in the warm sector is listed in the upper right-hand corner of each plot.

understand forecast sensitivities.

Many studies have evaluated storm forecast uncertainty arising from initially missing scales (e.g., Potvin et al., 2017) or imperceptibly small initial errors (e,g., Zhang et al., 2006, 2015; Markowski, 2020). Despite a focus on convective-scale uncertainties, modest large-scale errors can also severely limit forecast skill (e.g., Durran and Weyn, 2016) and should be represented in the initial conditions. While real-data cases initialized via ensemble data assimilation inherently include diverse meso- and synoptic-scale features, it remains a challenge to represent large scale uncertainties in idealized simulations which are typically initialized with a homogeneous environment. To address these uncertainties, studies often rely upon techniques such as displacing the source of convective initiation (e.g., Stratman et al., 2018; Markowski, 2020) or modifying the initial wind profile (e.g., Cintineo and Stensrud, 2013; Sherburn and Parker, 2019). Developing novel strategies to better represent IC uncertainties is expected to make ensemble spread more representative of the event uncertainty.

While idealized experiments are the focus of this study, physically realistic IC perturbations have the potential to benefit real-world applications. A significant challenge will be to apply these methods to full NWP models where the background environment is heterogeneous. One way forward is to consider the PCSC perturbations as pattern generator like those discussed by Palmer et al. (2009) for stochastic forcing in the boundary layer. Another method could be to coarse grain the perturbations, with appropriate scaling based upon a local and regional shear and stability, and add these into the model. Currently, operational ensemble forecast prediction systems add some form of uncertainty during model integration; the High Resolution Rapid Refresh (HRRR) ensemble analysis system uses stochastic perturbations of physics tendencies (Buizza et al., 1999; Palmer et al., 2009) and parameters to increase ensemble spread (Jankov et al., 2019). The combination of a more consistent initial uncertainty combined with stochastic methodologies, should provide the opportunity to maintain ensemble spread during integration more than either methodology can alone.

7 | ACKNOWLEDGEMENTS

This research was performed while the author held an NRC Research Associateship award at the National Severe Storms Laboratory. Funding was provided by the Verification of the Origins of Rotation in Tornadoes Experiment-Southeast (VORTEX-

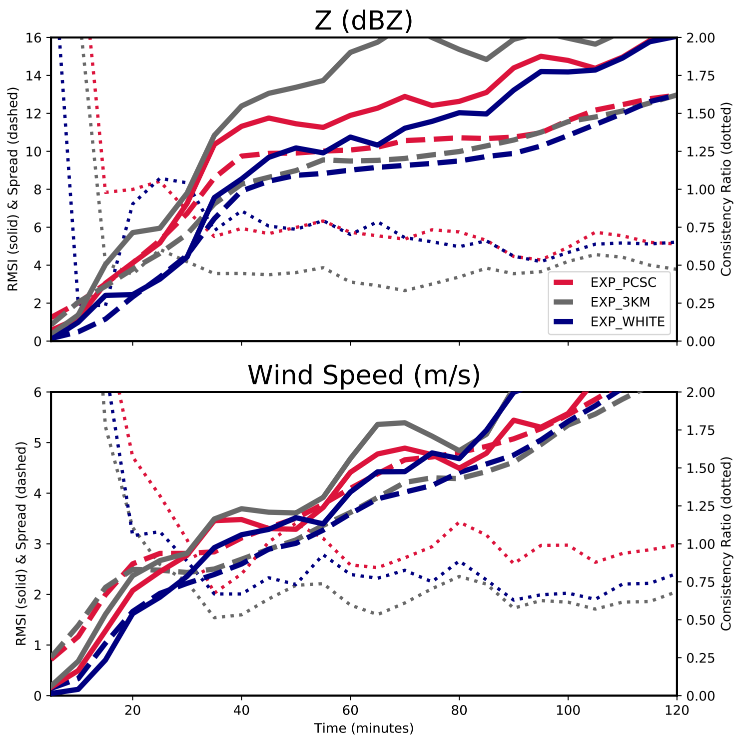

FIGURE 14 The RMSI (solid line) and ensemble spread (dashed lined) of (a) Z and (b) wind speed sampled at 0.5 km AGL for the supercell case. Statistics are considered where observations or ensemble mean Z exceed 15 dBZ. Consistency ratios (dotted line) are plotted on the secondary (right-hand) axis. Red, grey, and blue lines correspond with EXP_PCSC, EXP_3KM, and EXP_WHITE, respectively.

SE) and United States of America (VORTEX-USA) projects. Two anonymous reviewers provided helpful feedback that greatly improved the quality of this study. The authors thank Keith Sherburn and Matthew Parker, who provided the initial sounding and model settings for the QLCS case. Jeremy Gibbs provided code for the spectral density plots. Corey Potvin reviewed the manuscript and along with Paul Markowksi, Jeremy Gibbs, and Branden Katona provided useful insights that furthered this work. Valuable local computing assistance was provided by Gerry Creager, Jesse Butler, and Jeff Horn; additional computations were run on the schooner machine at the University of Oklahoma Supercomputing Center for Education and Research. Soundings and CAPE calculations are performed with metpy software.

REFERENCES

Adlerman, E. J., Droegemeier, K. K. and Davies-Jones, R. (1999) A Numerical Simulation of Cyclic Mesocyclogenesis. *Chemical Engineering Research and Design*, **56**, 2045–2069.

Aksoy, A., Dowell, D. C. and Snyder, C. (2009) A multicase comparative assessment of the ensemble Kalman filter for assimilation of radar observations. Part I: Storm-scale analyses. *Monthly Weather Review*, **137**, 1805–1824.

Benjamin, S. G., Dévényi, D., Weygandt, S. S., Brundage, K. J., Brown, J. M., Grell, G. A., Kim, D., Schwartz, B. E., Smirnova, T. G., Smith, T. L. and Manikin, G. S. (2004) An hourly assimilation-forecast cycle: The RUC. *Monthly Weather Review*, **132**, 495–518.

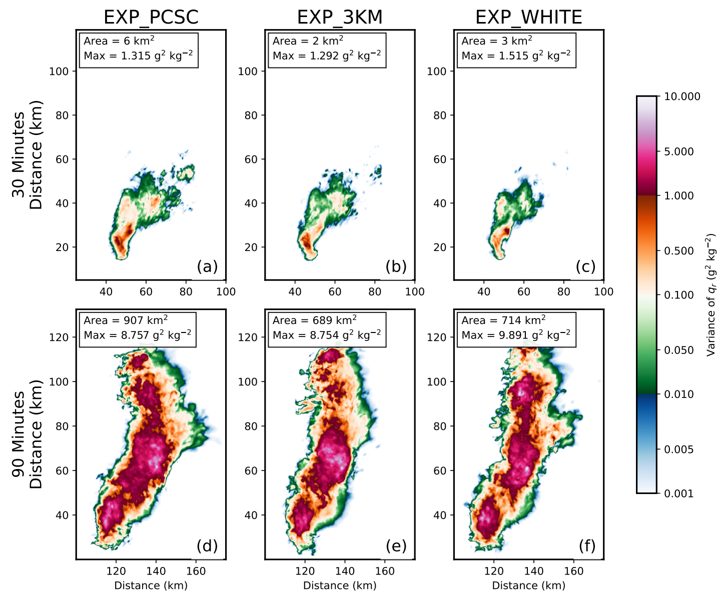

FIGURE 15 The ensemble variance of q_r at the lowest model level above the surface for (a, d) EXP_PCSC, (b, e) EXP_3KM, and (e, f) EXP_WHITE for the supercell case. Tables in the upper left-hand corner of each plot show areal coverage of grid points exceeding a high variance threshold (var(q_r) > 1.00 g^2 kg^{-2}) and maximum variance. Plots are centered upon the location of convection.

Brown, R. A. (1970) A Secondary Flow Model for the Planetary Boundary Layer. *Journal of the Atmospheric Sciences*, **27**, 742–757.

Bryan, G. H., Dahl, N. A., Nolan, D. S. and Rotunno, R. (2017) An eddy injection method for large-eddy simulations of Tornado-like vortices. *Monthly Weather Review*, **145**, 1937–1961.

Bryan, G. H. and Fritsch, J. M. (2002) A benchmark simulation for moist nonhydrostatic numerical models. *Monthly Weather Review*, **130**, 2917–2928.

Bryan, G. H., Rotunno, R. and Fritsch, J. M. (2007) Roll circulations in the convective region of a simulated squall line. *Journal of the Atmospheric Sciences*, **64**, 1249–1266.

Bryan, G. H., Wyngaard, J. C. and Fritsch, M. J. (2003) Resolution Requirements for the Simulation of Deep Moist Convection. *Monthly Weather Review*, **131**, 2394–2416.

Buizza, R., Hollingsworth, A., Lalaurette, F. and Ghelli, A. (1999) Probabilistic Predictions of Precipitation Using the ECMWF Ensemble Prediction System. *Weather and Forecasting*, **14**, 168 – 189.

Caya, A., Sun, J. and Snyder, C. (2005) A Comparison between the 4DVAR and the Ensemble Kalman Filter Techniques for. *Monthly Weather Review*, **133**, 3081–3094.

Cintineo, R. M. and Stensrud, D. J. (2013) On the predictability of supercell thunderstorm evolution. *Journal of the Atmospheric Sciences*, **70**, 1993–2011.

Clark, A. J., Gallus, W. A., Xue, M. and Kong, F. (2009) A Comparison of Precipitation Forecast Skill between Small Convection-Allowing and Large Convection-Parameterizing Ensembles. *Weather and Forecasting*, **24**, 1121–1140.

— (2010) Growth of Spread in Convection-Allowing and Convection-Parameterizing Ensembles. *Weather and Forecasting*, **25**, 594–612.

Coffer, B. E. and Parker, M. D. (2017) Simulated supercells in nontornadic and tornadic VORTEX2 environments. *Monthly Weather Review*, **145**, 149–180.

Coffer, B. E., Parker, M. D., Dahl, J. M., Wicker, L. J. and Clark, A. J. (2017) Volatility of tornadogenesis: An ensemble of simulated nontornadic and tornadic supercells in VORTEX2 environments. *Monthly Weather Review*, **145**, 4605–4625.

Crook, N. A. (1996) Sensitivity of Moist Convection Forced by Boundary Layer Processes to Low-Level Thermodynamic Fields. *Monthly Weather Review*, **124**, 1767–1785.

Dahl, J. M., Parker, M. D. and Wicker, L. J. (2014) Imported and storm-generated near-ground vertical vorticity in a simulated supercell. *Journal of the Atmospheric Sciences*, **71**, 3027–3051.

Dawson, D. T. I., Wicker, L. J., Mansell, E. R. and Tanamachi, R. L. (2012) Impact of the Environmental Low-Level Wind Profile on Ensemble Forecasts of the 4 May 2007 Greensburg, Kansas, Tornadic Storm and Associated Mesocyclones. *Monthly Weather Review*, **140**, 696–716.

Deardorff, J. W. (1980) Stratocumulus-Capped Mixed Layers Derived From a Three-Dimensional Model. *Boundary-Layer Meteorology*, **18**, 495–527.

Dowell, D., Wicker, L. J. and Snyder, C. (2011) Ensemble Kalman Filter Assimilation of Radar Observations of the 8 May 2003 Oklahoma City Supercell : Influences of Reflectivity Observations on Storm-Scale Analyses. *Monthly Weather Review*, **139**, 272–294.

Dowell, D., Wicker, L. J. and Stensrud, D. (2004) High-resolution analyses of the 8 May 2003 Oklahoma City storm. Part II: EnKF data assimilation and forecast experiments. In *22nd Conf. on Severe Local Storms*. Hyannis, MA: Amer. Meteor. Soc.

Dowell, D. C. and Wicker, L. J. (2009) Additive noise for storm-scale ensemble data assimilation. *Journal of Atmospheric and Oceanic Technology*, **26**, 911–927.

Durran, D. R. and Weyn, J. A. (2016) Thunderstorms do not get butterflies. *Bulletin of the American Meteorological Society*, **97**, 237–243.

Flora, M. L., Potvin, C. K. and Wicker, L. J. (2018) Practical predictability of supercells: Exploring ensemble forecast sensitivity to initial condition spread. *Monthly Weather Review*, **146**, 2361–2379.

Flournoy, M. D., Conigli, M. C., Rasmussen, E. N., Furtado, J. C. and Coffer, B. E. (2020) Modes of storm-scale variability and tornado potential in VORTEX2 near- And far-field tornadic environments. *Monthly Weather Review*, **148**, 4185–4207.

Frame, J. and Markowski, P. (2010) Numerical simulations of radiative cooling beneath the anvils of supercell thunderstorms. *Monthly Weather Review*, **138**, 3024–3047.

— (2013) Dynamical influences of anvil shading on simulated supercell thunderstorms. *Monthly Weather Review*, **141**, 2802–2820.

Gibbs, J. A. and Fedorovich, E. (2014) Comparison of convective boundary layer velocity spectra retrieved from large- eddy-simulation and Weather Research and Forecasting model data. *Journal of Applied Meteorology and Climatology*, **53**, 377–394.

Hastings, R. and Richardson, Y. (2016) Long-term morphological changes in simulated supercells following mergers with nascent supercells in directionally varying shear. *Monthly Weather Review*, **144**, 471–499.

Hohenegger, C. and Schär, C. (2007) Predictability and error growth dynamics in cloud-resolving models. *Journal of the Atmospheric Sciences*, **64**, 4467–4478.

Jankov, I., Beck, J., Wolff, J., Harrold, M., Olson, J. B., Smirnova, T., Alexander, C. and Berner, J. (2019) Stochastically perturbed parameterizations in an HRRR-based ensemble. *Monthly Weather Review*, **147**, 153–173.

Johnson, A. and Wang, X. (2016) A study of multiscale initial condition perturbation methods for convection-permitting ensemble forecasts. *Monthly Weather Review*, **144**, 2579–2604.

Johnson, A., Wang, X., Carley, J. R., Wicker, L. J. and Karstens, C. (2015) A comparison of multiscale GSI-based EnKF and 3DVar data assimilation using radar and conventional observations for midlatitude convective-scale precipitation forecasts. *Monthly Weather Review*, **143**, 3087–3108.

Jung, Y., Xue, M. and Tong, M. (2012) Ensemble Kalman Filter Analyses of the 29–30 May 2004 Oklahoma Tornadic Thunderstorm Using One- and Two-Moment Bulk Microphysics Schemes, with Verification against Polarimetric Radar Data. *Monthly Weather Review*, **140**, 1457–1475.

Kaiser, R. and Fedorovich, E. (1998) Turbulence spectra and dissipation rates in a wind tunnel model of the atmospheric convective boundary layer. *Journal of the Atmospheric Sciences*, **55**, 580–594.

Kelly, M. and Wyngaard, J. C. (2006) Two-dimensional spectra in the atmospheric boundary layer. *Journal of the Atmospheric Sciences*, **63**, 3066–3070.

Klees, A. M., Richardson, Y. P., Markowski, P. M., Weiss, C., Wurman, J. M. and Kosiba, K. K. (2016) Comparison of the tornadic and nontornadic supercells intercepted by VORTEX2 on 10 June 2010. *Monthly Weather Review*, **144**, 3201–3231.

Klemp, J. B. and Wilhelmson, R. B. (1978) The Simulation of Three-Dimensional Convective Storm Dynamics. *Journal of the Atmospheric Sciences*, **35**, 1070–1096.

Kolmogorov, A. N. (1941) Local structure of turbulence in the in- compressible fluid at very high Reynolds numbers. *Dokl. Akad. Nauk S.S.S.R.*, **30**, 299–303.

Lawson, J. R. (2019) Predictability of Idealized Thunderstorms in Buoyancy–Shear Space. *Journal of the Atmospheric Sciences*, **76**, 2653–2672.

Loken, E. D., Clark, A. J., Xue, M. and Kong, F. (2019) Spread and Skill in Mixed- and Single-Physics Convection-Allowing Ensembles. *Weather and Forecasting*, **34**, 305–330.

Lorenz, E. N. (1969) The predictability of a flow which possesses many scales of motion. *Tellus A*, **1**.

Mansell, E. R., Ziegler, C. and Bruning, E. (2010) Simulated Electrification of a Small Thunderstorm with Two-Moment Bulk Microphysics. *Journal of Atmospheric Sciences*, **67**, 171–194.

Markowski, P. M. (2016) An idealized numerical simulation investigation of the effects of surface drag on the development of near-surface vertical vorticity in supercell thunderstorms. *Journal of the Atmospheric Sciences*, **73**, 4349–4385.

— (2020) What is the intrinsic predictability of tornadic supercell thunderstorms? *Monthly Weather Review*, **148**, 3157–3180.

Markowski, P. M. and Bryan, G. H. (2016) LES of laminar flow in the PBL: A potential problem for convective storm simulations. *Monthly Weather Review*, **144**, 1841–1850.

Markowski, P. M. and Harrington, J. Y. (2005) A simulation of a supercell thunderstorm with emulated radiative cooling beneath the anvil. *Journal of the Atmospheric Sciences*, **62**, 2607–2617.

Markowski, P. M., Straka, J. M., Rasmussen, E. N. and Blanchard, D. O. (1998) Variability of storm-relative helicity during VORTEX. *Monthly Weather Review*, **126**, 2959–2971.

Martin, W. J. and Xue, M. (2006) Sensitivity analysis of convection of the 24 May 2002 IHOP case using very large ensembles. *Monthly Weather Review*, **134**, 192–207.

May, R. M., Arms, S. C., Marsh, P., Bruning, E. and Leeman, J. R. (2008) MetPy: A Python package for meteorological data. URL: `https://github.com/Unidata/MetPy`.

McCaul, E. W. J. and Weisman, M. L. (2001) The sensitivity of simulated supercell structure and intensity to variations in the shapes of environmental buoyancy and shear profiles. *Monthly Weather Review*, **129**, 664–687.

Nowotarski, C. J. and Markowski, P. M. (2016) Modifications to the near-storm environment induced by simulated supercell thunderstorms. *Monthly Weather Review*, **144**, 273–293.

Palmer, T., Buizza, R., Doblas-Reyes, F., Jung, T., Leutbecher, M., Shutts, G., Steinheimer, M. and Weisheimer, A. (2009) Stochastic parametrization and model uncertainty. 42. URL: https://www.ecmwf.int/node/11577.

Potvin, C. K. and Flora, M. L. (2015) Sensitivity of Idealized Supercell Simulations to Horizontal Grid Spacing: Implications for Warn-on-Forecast. *Monthly Weather Review*, **143**, 2998–3024.

Potvin, C. K., Murillo, E. M., Flora, M. L. and Wheatley, D. M. (2017) Sensitivity of supercell simulations to initial-condition resolution. *Journal of the Atmospheric Sciences*, **74**, 5–26.

Potvin, C. K., Wicker, L. J., Biggerstaff, M. I., Betten, D. and Shapiro, A. (2013) Comparison between dual-doppler and EnKF storm-scale wind analyses: The 29-30 May 2004 Geary, Oklahoma, supercell thunderstorm. *Monthly Weather Review*, **141**, 1612–1628.

Roberts, B., Xue, M., Schenkman, A. D. and Dawson, D. T. (2016) The role of surface drag in tornadogenesis within an idealized supercell simulation. *Journal of the Atmospheric Sciences*, **73**, 3371–3395.

Romine, G. S., Schwartz, C. S., Berner, J., Fossell, K. R., Snyder, C., Anderson, J. L. and Weisman, M. L. (2014) Representing forecast error in a convection-permitting ensemble system. *Monthly Weather Review*, **142**, 4519–4541.

Romine, G. S., Schwartz, C. S., Snyder, C., Anderson, J. L. and Weisman, M. L. (2013) Model bias in a continuously cycled assimilation system and its influence on convection-permitting forecasts. *Monthly Weather Review*, **141**, 1263–1284.

Rotunno, R. and Klemp, J. B. (1985) On the Rotation and Propagation of Simulated Supercell Thunderstorms. *Jounal of the Atmospheric Sciences*, **42**, 271–292.

Schenkman, A. D., Xue, M. and Hu, M. (2014) Tornadogenesis in a high-resolution simulation of the 8 May 2003 Oklahoma City supercell. *Journal of the Atmospheric Sciences*, **71**, 130–154.

Schenkman, A. D., Xue, M. and Shapiro, A. (2012) Tornadogenesis in a Simulated Mesovortex within a Mesoscale Convective System. *Journal of the Atmospheric Sciences*, **69**, 3372–3390. URL: http://dx.doi.org/10.1175/JAS-D-12-038.1.

Schwartz, C. S., Romine, G. S., Sobash, R. A., Fossell, K. R. and Weisman, M. L. (2015) NCAR ' s Experimental Real-Time Convection-Allowing Ensemble Prediction System. *Weather and Forecasting*, **30**, 1645–1654.

Sherburn, K. D. and Parker, M. D. (2019) The development of severe vortices within simulated high-shear, Low-CAPE convection. *Monthly Weather Review*, **147**, 2189–2216.

Skamarock, W. C. (2004) Evaluating mesoscale NWP models Using Kinetic Energy Spectra. *Monthly Weather Review*, **132**, 3019–3032.

Skinner, P. S., Weiss, C. C., French, M. M., Bluestein, H. B., Markowski, P. M. and Richardson, Y. P. (2014) VORTEX2 observations of a low-level mesocyclone with multiple internal rear-flank downdraft momentum surges in the 18 May 2010 Dumas, Texas, supercell. *Monthly Weather Review*, **142**, 2935–2960.

Snook, N., Jung, Y., Brotzge, J., Putnam, B. J. and Xue, M. (2016) Prediction and Ensemble Forecast Verification of Hail in the Supercell Storms of 20 May 2013. *Weather and Forecasting*, **4**, 811–825.

Snyder, C. and Zhang, F. (2003) Assimilation of Simulated Doppler Radar Observations with an Ensemble Kalman Filter. *Monthly Weather Review*, **131**, 1663–1677.

Sobash, R. A. and Stensrud, D. J. (2013) The impact of covariance localization for radar data on EnKF analyses of a developing MCS: Observing system simulation experiments. *Monthly Weather Review*, **141**, 3691–3709.

Sobash, R. A. and Wicker, L. J. (2015) On the impact of additive noise in storm-scale EnKF experiments. *Monthly Weather Review*, **143**, 3067–3086.

Stratman, D. R., Potvin, C. K. and Wicker, L. J. (2018) Correcting storm displacement errors in ensembles using the feature alignment technique (FAT). *Monthly Weather Review*, **146**, 2125–2145.

Stull, R. B. (1988) *An Introduction to Boundary Layer Meteorology*. Springer.

Tanamachi, R. L., Heinselman, P. L. and Wicker, L. J. (2015) Impacts of a storm merger on the 24 May 2011 El Reno, Oklahoma, tornadic supercell. *Weather and Forecasting*, **30**, 501–524.

Tennekes, H. and Lumley, J. L. (1972) *A First Course in Turbulence*. The MIT Press.

Tong, M. and Xue, M. (2005) Ensemble Kalman Filter Assimilation of Doppler Radar Data with a Comprssible Nonhydrostatic Model: OSS Experiments. *Monthly Weather Review*, **133**, 1789–1807.

Weckwerth, T. M., Murphey, H. V., Flamant, C., Goldstein, J. and Pettet, C. R. (2008) An observational study of convection initiation on 12 June 2002 during IHOP_2002. *Monthly Weather Review*, **136**, 2283–2304.

Weisman, M. L. and Klemp, J. B. (1982) The dependence of numerically simulated convective storms on vertical wind shear and buoyancy. *Monthly Weather Review*, **110**, 504–520. URL: `http://journals.ametsoc.org/doi/abs/10.1175/1520-0493(1982)110{\%}3C0504:TDONSC{\%}3E2.0.CO{\%}3B2`.

— (1984) The structure and classification of numerically simulated convective storms in directionally varying wind shears. *Monthly Weather Review*, **112**, 2479–2498. URL: `http://journals.ametsoc.org/doi/abs/10.1175/1520-0493(1984)112{\%}3C2479:TSACON{\%}3E2.0.CO{\%}3B2`.

Wicker, L. J. and Wilhelmson, R. B. (1995) Simulation and Analysis of Tornado Development and Decay within a Three-Dimensional Supercell Thunderstorm. *Journal of Atmospheric Sciences*, **52**, 2675–2703.

Wilson, J. W., Foote, G. B., Crook, N. A., Fankhauser, J. C., Wade, C. G., Tuttle, J. D. and Mueller, C. K. (1992) The Role of Boundary-Layer Convergence Zones and Horizontal Folls in the Initiation of Thunderstorms: A Case Study. *Monthly Weather Review*, **120**, 1785–1815.

Wurman, J., Richardson, Y., Alexander, C., Weygandt, S. and Zhang, P. F. (2007) Dual-Doppler and single-Doppler analysis of a tornadic storm undergoing mergers and repeated tornadogenesis. *Monthly Weather Review*, **135**, 736–758.

Yussouf, N., Mansell, E. R., Wicker, L. J., Wheatley, D. and Stensrud, D. (2013) The Ensemble Kalman Filter Analyses and Forecasts of the 8 May 2003 Oklahoma City Tornadic Supercell Storm Using Single- and Double-Moment Microphysics Schemes. *Monthly Weather Review*, **141**, 3388–3412.

Zhang, F., Bei, N., Rotunno, R., Snyder, C. and Epifanio, C. C. (2007) Mesoscale predictability of moist baroclinic waves: Convection-permitting experiments and multistage error growth dynamics. *Journal of the Atmospheric Sciences*, **64**, 3579–3594.

Zhang, F., Odins, A. M. and Nielsen-Gammon, J. W. (2006) Mesoscale predictability of an extreme warm-season precipitation event. *Weather and Forecasting*, **21**, 149–166.

Zhang, F., Snyder, C. and Sun, J. (2004) Impacts of Initial Estimate and Observation Availability on Convective-Scale Data Assimilation with an Ensemble Kalman Filter. *Monthly Weather Review*, **132**, 1238–1253.

Zhang, J., Howard, K., Langston, C., Kaney, B., Qi, Y., Tang, L., Grams, H., Wang, Y., Cocks, S., Martinaitis, S. M., Arthur, A., Cooper, K., Brogden, J. and Kitzmiller, D. (2016) Multi-Radar Multi-Sensor (MRMS) Quantitative Precipitation Estimation Initial Operating Capabilities. *Bulletin of the American Meteorological Society*, **97**, 621–638.

Zhang, Y., Zhang, F., Stensrud, D. J. and Meng, Z. (2015) Practical predictability of the 20 May 2013 tornadic thunderstorm event in Oklahoma: sensitivity to synoptic timing and topographical influence. *Monthly Weather Review*, **143**, 2973–2997.